Advances in Atmospheric Sciences
Impact Factor: 5.8
E-alert
ISSN 0256-1530
CN 11-1925/O4

The First Global Map of Atmospheric Ammonia (NH_3) as Observed by the HIRAS/FY-3D Satellite

Minqiang ZHOU, Zhili DENG, Charles ROBERT, Xingying ZHANG, Lu ZHANG, Yapeng WANG, Chengli QI, Pucai WANG, Martine De MAZIRE

Citation: Zhou, M. Q., and Coauthors 2024: The First Global Map of Atmospheric Ammonia (NH_3) as Observed by the HIRAS/FY-3D Satellite, *Adv. Atmos. Sci.*, 41, 520-531. doi: 10.1007/s00376-023-3059-9.

View online: https://doi.org/10.1007/s00376-023-3059-9

ADVANCES IN ATMOSPHERIC SCIENCES, VOL. 41, MARCH 2024, 379–390

• **Original Paper** •

The First Global Map of Atmospheric Ammonia (NH_3) as Observed by the HIRAS/FY-3D Satellite

Minqiang ZHOU[1,2], Zhili DENG[3], Charles ROBERT[2], Xingying ZHANG[*4], Lu ZHANG[3], Yapeng WANG[3], Chengli QI[3], Pucai WANG[1,5], and Martine De MAZIÈRE[2]

[1]*Institute of Atmospheric Physics*, *Chinese Academy of Sciences*, *Beijing* 100029, *China*

[2]*Royal Belgian Institute for Space Aeronomy (BIRA-IASB)*, *Brussels* 1180, *Belgium*

[3]*National Satellite Meteorology Center*, *China Meteorological Administration*, *Beijing* 100081, *China*

[4]*Department of Science & Technology and Climate Change*, *China Meteorological Administration*, *Beijing* 100081, *China*

[5]*University of Chinese Academy of Sciences*, *Beijing* 100049, *China*

(Received 21 March 2023; revised 13 July 2023; accepted 14 July 2023)

ABSTRACT

Atmospheric ammonia (NH_3) is a chemically active trace gas that plays an important role in the atmospheric environment and climate change. Satellite remote sensing is a powerful technique to monitor NH_3 concentration based on the absorption lines of NH_3 in the thermal infrared region. In this study, we establish a retrieval algorithm to derive the NH_3 column from the Hyperspectral Infrared Atmospheric Sounder (HIRAS) onboard the Chinese FengYun (FY)-3D satellite and present the first atmospheric NH_3 column global map observed by the HIRAS instrument. The HIRAS observations can well capture NH_3 hotspots around the world, e.g., India, West Africa, and East China, where large NH_3 emissions exist. The HIRAS NH_3 columns are also compared to the space-based Infrared Atmospheric Sounding Interferometer (IASI) measurements, and we find that the two instruments observe a consistent NH_3 global distribution, with correlation coefficient (R) values of 0.28–0.73. Finally, some remaining issues about the HIRAS NH_3 retrieval are discussed.

Key words: ammonia, HIRAS/FY-3D satellite, thermal-infrared observation, remote sensing, optimal estimation method

Citation: Zhou, M. Q., and Coauthors, 2024: The first global map of atmospheric ammonia (NH_3) as observed by the HIRAS/FY-3D satellite. *Adv. Atmos. Sci.*, **41**(3), 379−390, https://doi.org/10.1007/s00376-023-3059-9.

Article Highlights:

- A full-physical retrieval algorithm is established based on the optimal estimation method to retrieve the atmospheric NH_3 column.
- The first NH_3 column global map is successfully derived from the HIRAS/FY-3D satellite thermal-infrared spectra.
- Positive correlations with R-values of 0.28–0.73 are found between HIRAS and IASI NH_3 column measurements and the differences are within their estimated uncertainties.

1. Introduction

Atmospheric ammonia (NH_3) is an important trace gas that causes environmental problems and harms human health. As the most abundant alkaline gas, NH_3 reacts with atmospheric sulfuric acid and nitric acid, and it is a major source of aerosols (Na et al., 2007; Hao et al., 2020; Bao et al., 2021). The ammonium aerosols change the reflectivity of the Earth's surface and play a significant role in the radiance balance of the Earth's system (Xu and Penner, 2012). When aerosols are deposited on water surfaces, eutrophication can occur, damaging the aquatic ecosystem (Mahowald et al., 2017). Guo et al. (2020) estimated that ammonia-related aerosols could lead to 36 billion dollars of public health loss per year in the United States.

Ammonia (NH_3) in the atmosphere is mainly emitted from livestock animal wastes and fertilizer productions/applications (~85%), and partly from industrial manufacture, biomass burning, transports, plant decomposition, and volatilization from oceans and soils (Behera et al., 2013; Zhu et al., 2015; Van Damme et al., 2018). Due to its importance, NH_3 emission inventories have been developed (Bouwman et al., 1997; Crippa et al., 2020). However, the current NH_3 emissions remain highly uncertain at a global scale due to a lack of NH_3 observations (Luo et al., 2022). It is quite dif-

* Corresponding author: Xingying ZHANG
Email: zxy@cma.gov.cn

ficult to measure the NH_3 concentration by in situ techniques, as the NH_3 molecules will adsorb to the inlet and other surfaces of the in situ instrument (Twigg et al., 2022).

Satellite remote sensing techniques using the specific absorption lines of NH_3 in the thermal infrared spectral region can provide global NH_3 column measurements. The first global NH_3 map was successfully derived from the Infrared Atmospheric Sounding Interferometer (IASI) carried on the MetOp-A satellite (Clarisse et al., 2009). Later, NH_3 columns were also derived from several other hyperspectral infrared satellites, e.g., the Cross-track Infrared Sounder (CrIS) and the Thermal And Near infrared Sensor for carbon Observations-Fourier Transform Spectrometer (TANSO-FTS) (Shephard and Cady-Pereira, 2015; Someya et al., 2020). The NH_3 columns derived from satellite IASI and CrIS measurements have been compared and validated with ground-based Fourier Transform Spectrometer (FTS) retrievals, and the results show that there is a good correlation between ground-based and satellite NH_3 measurements and the bias between them is typically within their estimated retrieval uncertainties (Dammers et al., 2016, 2017).

In November 2017, the Hyperspectral Infrared Atmospheric Sounder (HIRAS) was launched into a sun-synchronous polar orbit at 863 km above the ground onboard the meteorological FengYun (FY)-3D satellite. It was the first Chinese satellite sensor to provide nadir hyperspectral infrared spectra of the upwelling radiance between 650 and 2550 cm^{-1} (Yang et al., 2019). The performance of HIRAS has been well evaluated and calibrated in the optical laboratory before launch, and in space after launch (Qi et al., 2020; Wu et al., 2020). The brightness temperature noise level of the HIRAS spectra is about 0.15–0.4 K at 280 K (Qi et al., 2020), which is slightly larger than the IASI noise level of about 0.1–0.2 K at 280 K (Hilton et al., 2012). Atmospheric temperature and water vapor have been successfully derived from the HIRAS spectra (Zhang et al., 2021; Li et al., 2022). However, until now, the HIRAS spectra have never been used to retrieve atmospheric NH_3 concentrations.

In this study, we establish a retrieval algorithm to derive the NH_3 column from the HIRAS observed spectra and present the first HIRAS NH_3 global map. Section 2 describes the satellite data and the retrieval method. In section 3, we show the retrieval results and the comparisons between HIRAS and IASI NH_3 column retrievals. After that, the current issues affecting HIRAS NH_3 retrieval are discussed in section 4. Finally, conclusions are drawn in section 5.

2. Data and retrieval methods

2.1. *HIRAS observed spectra*

HIRAS is a Fourier transform spectrometer that records infrared spectra emitted by the Earth, its atmosphere, and the solar component. One HIRAS cross-track scan sequence has 33 measurements, including 29 Earth Scenes, 2 Deep Space, and 2 Internal Calibration Target observations (Wu et al., 2020). With a wide swath width of about 2250 km, it offers near-global coverage twice a day, with overpass times at 0130 and 1330 (local solar time). The field of view (FOV) of each HIRAS footprint is 1.1°, corresponding to a 16-km diameter projection on the ground at nadir (Qi et al., 2020). There are three bands observed by the HIRAS sensor: the long wave IR (LWIR) band from 650 to 1135 cm^{-1}, the middle wave IR (MWIR) band from 1210 to 1750 cm^{-1}, and the short wave IR (SWIR) band from 2155 to 2550 cm^{-1}. All bands are recorded at the same full spectral resolution of 0.625 cm^{-1}, corresponding to a maximum optical path difference (MOPD) of 0.8 cm. For the MWIR and SWIR bands, HIRAS also provides data with spectral resolutions of 1.25 and 2.5 cm^{-1}, respectively. As the NH_3 absorption lines lie mainly in the LWIR (Gordon et al., 2022), only the HIRAS LWIR spectra with a spectral resolution of 0.625 cm^{-1} are used hereafter.

Figure 1a shows a typical HIRAS LWIR spectrum, along with the NH_3 retrieval window. The HIRAS spectra used in this study cover January and July 2020 (2 months; 62 days). According to the HITRAN 2020 spectroscopy, relatively strong NH_3 absorption lines are found near 930 and 967 cm^{-1}. We tested both the 925–935 cm^{-1} and 960–970 cm^{-1} spectral windows to check their sensitivity to the NH_3 columns. In the former window, we found that there are many strong CO_2 and H_2O lines that contaminate the NH_3 signal. Therefore, the latter (960–970 cm^{-1}) window was selected for retrieval. Figure 2 shows a typical transmittance spectrum from the surface to the top of the atmosphere between 960 and 970 cm^{-1} using the US standard atmosphere (NOAA, 1976). Although there is still some interference from CO_2, H_2O, and O_3; NH_3 absorption lines are less affected by them, especially near 965.5 and 967.3 cm^{-1}.

To reduce the impact from clouds, we only perform the NH_3 retrieval under clear-sky conditions. The medium-resolution spectral imager-2 (MERSI-2) sensor onboard the FY-3D satellite provides cloud mask products with a 250-m spatial resolution (Xian et al., 2021). We calculate the cloud fraction based on the MERSI-2 cloud measurements for each HIRAS observation and select the clear-sky HIRAS measurements (cloud fraction equal to 0). The cloud masking procedure used here is the same as in Li et al. (2022).

2.2. *Optimal estimation method*

The optimal estimation method (OEM; Rodgers, 2000) is applied to retrieve the NH_3 column from the observed HIRAS spectra. A cost function $[\mathbf{J}(\mathbf{x})]$ is defined by Eq. (1):

$$\mathbf{J}(\mathbf{x}) = [\mathbf{y} - \mathbf{F}(\mathbf{x},\mathbf{b})]^{\mathrm{T}}\mathbf{S}_{\epsilon}^{-1}[\mathbf{y} - \mathbf{F}(\mathbf{x},\mathbf{b})] + [\mathbf{x} - \mathbf{x}_{\mathrm{a}}]^{\mathrm{T}}\mathbf{S}_{\mathrm{a}}^{-1}[\mathbf{x} - \mathbf{x}_{\mathrm{a}}] , \quad (1)$$

where $\mathbf{y}$ is the observed spectra; $\mathbf{F}(\mathbf{x},\mathbf{b})$ is the forward model to simulate spectra; $\mathbf{x}$ is the state vector (retrieved parameters); $\mathbf{b}$ represents the model parameters that are not retrieved, such as the surface emissivity, temperature profile, and satellite-Earth geometry; subscripts a and ϵ represent

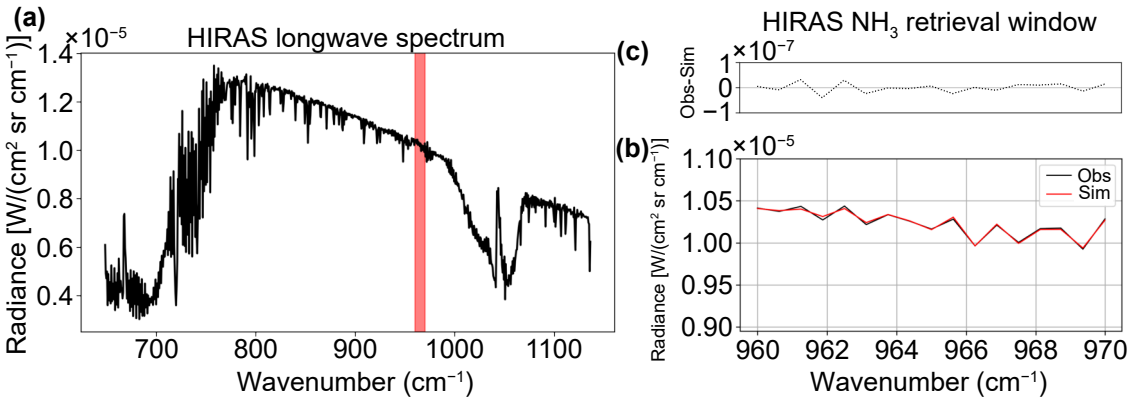

Fig. 1. (a) A typical HIRAS observed spectra in the long wavelength range (648–1136 cm^{-1}; spectral resolution of 0.625 cm^{-1}) at 18.72°N, 70.50°E, for a satellite zenith angle of 3.27° and a solar zenith angle of 45.25°. The NH_3 retrieval window (960–970 cm^{-1}) is marked by a red shadow. (b) The observed (Obs) and simulated (Sim) spectra, and (c) the residual of the fitted spectrum (Obs – Sim).

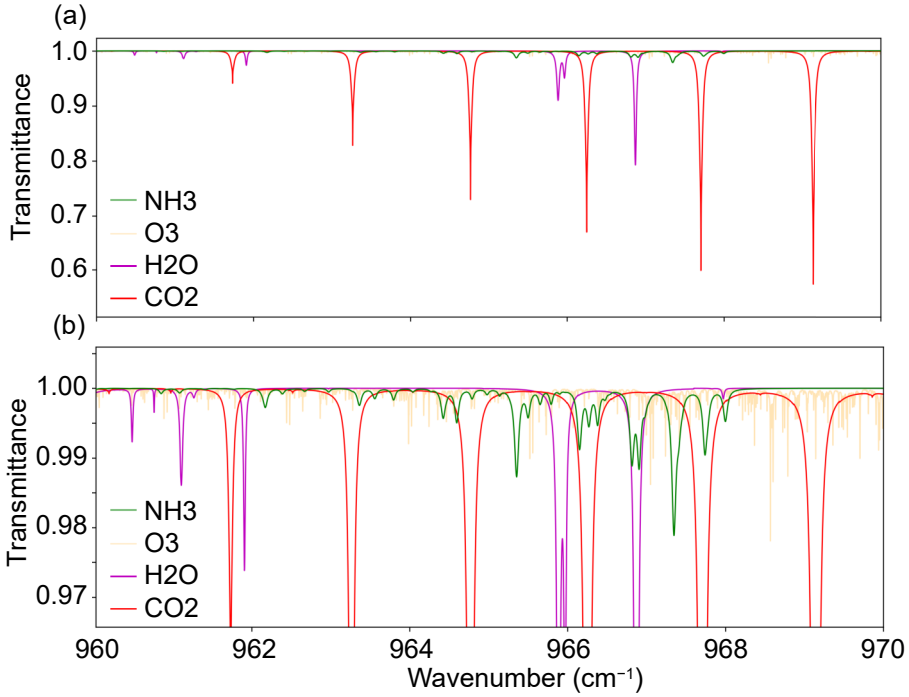

Fig. 2. (a) The transmittances of the main species (CO_2, H_2O, O_3, and NH_3) in the NH_3 retrieval window, and (b) a zoom window in the transmittance range between 0.965 and 1.00 to establish a better view of NH_3 absorption lines.

the prior and the measurement noise, respectively; $\mathbf{x}_a$ is the prior, presenting the best estimation of the state vector based on the a priori knowledge; $\mathbf{S}_\epsilon$ is the measurement covariance matrix, determined by the signal-to-noise-ratio (SNR) of the HIRAS observed spectrum (the diagonal values of the $\mathbf{S}_\epsilon$ are calculated as $1/\mathrm{SNR}^2$, and the non-diagonal values are set to 0); $\mathbf{S}_a$ is the a priori covariance matrix of the state vector, derived from an atmospheric chemistry transport model. The Newton iteration is applied to find the approximation of the true state which agrees best with both the measurement and the a priori information. It follows:

$$\mathbf{x}_{i+1} = \mathbf{x}_a + \mathbf{G}_i\left[\mathbf{y} - \mathbf{F}(\mathbf{x}_i, \mathbf{b}) + \mathbf{K}_i(\mathbf{x}_i - \mathbf{x}_a)\right], \tag{2}$$

$$\mathbf{G}_i = \left(\mathbf{S}_a^{-1} + \mathbf{K}_i{}^{\mathrm{T}}\mathbf{S}_\varepsilon^{-1}\mathbf{K}_i\right)^{-1}\mathbf{K}_i{}^{\mathrm{T}}\mathbf{S}_\varepsilon^{-1}, \tag{3}$$

where $\mathbf{G}$ is the contribution matrix, $\mathbf{K}$ is the Jacobian matrix, representing the sensitivity of the observed spectra to the parameters, and subscript i is the iteration index. Finally, the optimal state vector ($\widehat{\mathbf{x}}$) is given by Eq. (4):

$$\widehat{\mathbf{x}} = \mathbf{x}_a + \widehat{\mathbf{G}}\widehat{\mathbf{K}}(\mathbf{x}_t - \mathbf{x}_a) + \epsilon = \mathbf{x}_a + \mathbf{A}(\mathbf{x}_t - \mathbf{x}_a) + \epsilon, \tag{4}$$

where **A** is the averaging kernel matrix, representing the sensitivity of the retrieved parameters to the true state; ϵ is the retrieval uncertainty.

Table 1 lists the parameters in the state vector (**x**), together with both their a priori and variance settings. Apart from the NH_3 column, the columns of the interfering species (CO_2, H_2O, and O_3) are retrieved as well. In addition, the spectral shift and the surface temperature are included. Since the spatiotemporal variations of the H_2O column and the surface temperature are very large, their a priori values are derived from the ERA5 hourly reanalysis data (Hersbach et al., 2020).

2.3. *The forward model*

We use the ASIMUT model to simulate the infrared radiance transmitted from the Earth's surface to the HIRAS satellite sensor. The ASIMUT is a radiative transfer model (Vandaele et al., 2006) developed by the Royal Belgian Institute for Space Aeronomy (BIRA-IASB) which calculates the spectrum and analytical derivation of the Jacobians. The ASIMUT code has been applied for the dust and methane retrievals from the IASI satellite (Vandenbussche et al., 2013; De Wachter et al., 2017). The ASIMUT software has been coupled to the SPHER/TMATRIX (Mishchenko and Travis, 1998) and (V)LIDORT (Spurr, 2008) to compute the atmospheric scatterings.

In the NH_3 retrieval window (960–970 cm^{-1}), we neglect the scattering and consider the thermal emissions under local thermodynamical equilibrium. The line-by-line (LBL) method to calculate the cross-sections was implemented in the ASIMUT model, but it consumes large computing resources. To speed up the retrieval, we create look-up-tables (LUTs) for CO_2, H_2O, O_3, and NH_3 cross-sections in the spectral range from 900 to 1000 cm^{-1} based on the HITRAN 2020 database (Gordon et al., 2022), for various pressures (between 7×10^{-4} hPa and 1081 hPa) and temperatures (between 148 and 328 K). Numerous simulations with different pressure and temperature conditions have been carried out with both the LBL method and the LUT method, and the relative radiance differences between the LBL and LUT simulations are all within 0.005%, which is much smaller than the noise level of the HIRAS spectra.

The ASIMUT model includes 39 vertical layers between the surface and the top of the atmosphere (40 vertical levels: 0.0, 0.1, 0.3, 0.5, 0.7, 0.9, 1.0, 1.3, 1.5, 1.75, 2.0, 2.5, 3.2, 3.75, 4.5, 5.0, 6.0, 7.0, 8.0, 9.0, 10.0, 11.0, 12.0, 13.0, 14.0, 15.0, 17.0, 19.0, 21.0, 23.0, 25.0, 27.0, 30.0, 35.0, 40.0, 45.0, 50.0, 60.0, 70.0, and 100.0 km). The global spectrally dependent surface emissivity datasets are provided by Zhou et al. (2011). The HIRAS instrument line shape (ILS) has been taken into account in the forward model, which is characterized by a sinc function with a 0.625 cm^{-1} spectral resolution.

2.4. *A priori profile*

The Copernicus Atmosphere Monitoring Service (CAMS) global ECMWF Atmospheric Composition Reanalysis 4 (EAC4) model simulations are applied to generate the a priori information of NH_3. The CAMS EAC4 model has a horizontal resolution of $0.75° \times 0.75°$, with 60 model vertical levels between the ground and 0.2 hPa. The CAMS model uses anthropogenic emissions from the MACCity inventory (Stein et al., 2014), fire emissions from the Global Fire Assimilation System (GFAS) (Kaiser et al., 2012), and the Model of Emissions of Gases and Aerosols from Nature (MEGAN) driven by the MERRA reanalyzed meteorology to generate the monthly mean volatile organic compound emissions (Sindelarova et al., 2014). For more information about the CAMS model simulations refer to Inness et al. (2019) and the references therein. Previous studies demonstrate that there are large day-to-day and month-to-month variabilities of NH_3 globally (Van Damme et al., 2015; Wang et al., 2021). Therefore, for the HIRAS NH_3 retrieval, we use the CAMS model monthly means between 2015 and 2020 (6 years) to generate the a priori profile of NH_3. Moreover, the standard deviation (std) of the daily NH_3 concentration is calculated in each grid cell to set the variability of the NH_3 (Sa $= 1\sigma^2$). Figure 3 shows the CAMS simulated NH_3 mole fraction near the surface (model bottom level). The NH_3 mole fractions are relatively high in Southeast Asia, South Asia, Europe, Australia, North America, and South America, and the NH_3 mole fractions are relatively low above the ocean and in the polar region, which is generally consistent with the IASI satellite observations (Van Damme et al., 2015). Figure 4a shows typical NH_3 vertical profiles over land and ocean derived from the CAMS model. The NH_3 mole fraction generally decreases with altitude and becomes less than 0.01 ppb above 10 km.

2.5. *Vertical sensitivity*

As shown in Table 1, we perform the column retrieval (only a scaling factor of NH_3 column in the state vector) for

Table 1. The state vector (**x**) together with their prior and variance (1σ) in the HIRAS NH_3 retrieval algorithm.

Retrieved parameters (**x**)	Prior	1σ
NH_3 column	CAMS model	SD of CAMS monthly means
O_3 column	CAMS model	50%
CO_2 column	Carbon Tracker	10%
H_2O column	ERA5 reanalysis data	100%
Surface temperature	ERA5 reanalysis data	3%
Spectral shift	0	10%

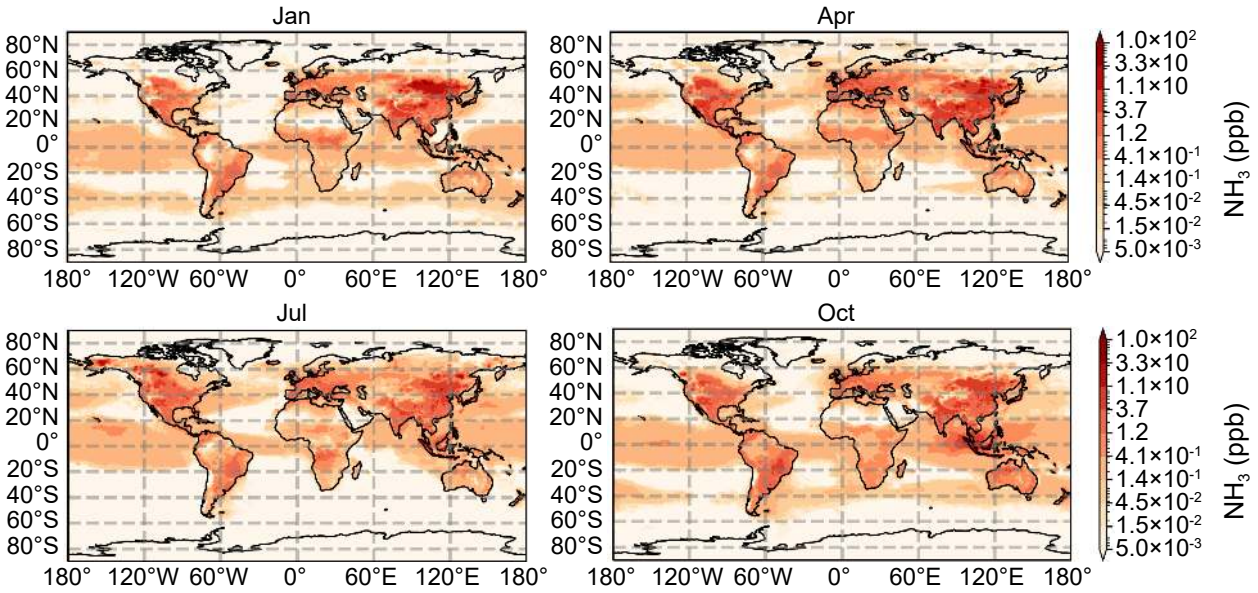

Fig. 3. The CAMS model global simulated NH_3 mole fraction near the surface in January, April, July, and October between 2015 and 2020.

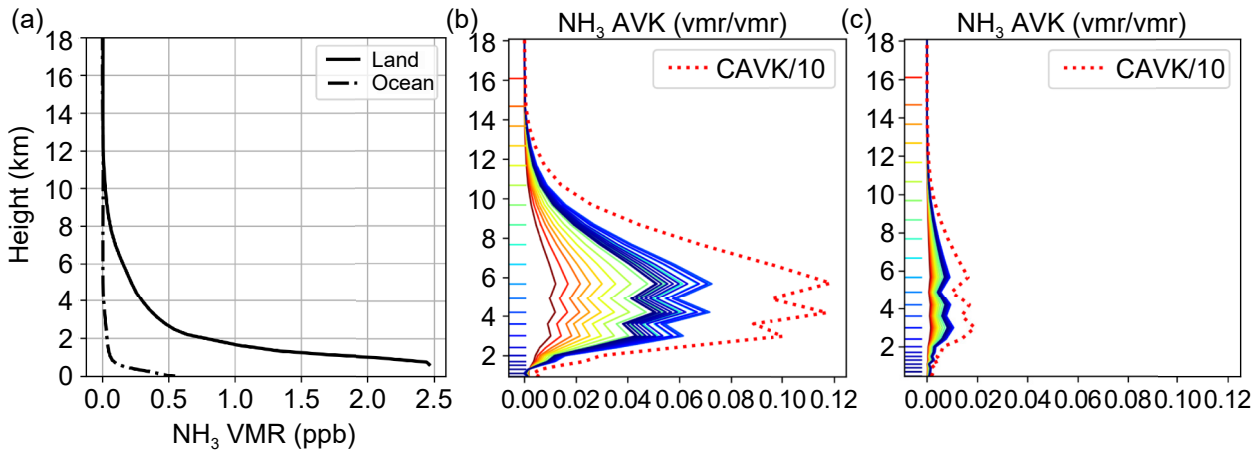

Fig. 4. Typical NH_3 vertical profiles from the CAMS model over land and ocean. (a) Typical averaging kernel matrix (solid lines; lines are colored with different altitudes; in units of ppb $(ppb)^{-1}$ and column averaging kernel scaled with 0.1 (red dashed line; in units of (molecules cm^{-2}) $(molecules\ cm^{-2})^{-1}$ of the HIRAS NH_3 retrieval over (b) land and (c) ocean.

the HIRAS NH_3 retrieval. To understand the vertical sensitivity of the NH_3 retrieved column, we carried out profile retrieval for NH_3 above several areas, such as in India and the tropical ocean, to derive the NH_3 profile averaging kernel (**AVK**) matrix in units of ppb $(ppb)^{-1}$. Note that we have tuned the Sa values to make the sum of the **AVK** matrix (DOF) from the profile retrieval close to what we get from the column retrieval. Then the column-averaging kernel (**CAVK**) is calculated based on the **AVK** matrix as follows:

$$\mathbf{x}_{r,p} = \mathbf{x}_{a,p} + \mathbf{AVK}(\mathbf{x}_{t,p} - \mathbf{x}_{a,p}), \quad (5)$$

$$TC_r = TC_a + \mathbf{CAVK} \cdot (\mathbf{PC}_t - \mathbf{PC}_a), \quad (6)$$

$$\mathbf{CAVK}_j = \sum_{i=1}^{n} \mathbf{AVK}\left(\mathbf{PC}_{air} \otimes \frac{1}{\mathbf{PC}_{air}}\right)_{ij}, \quad j = 1, \cdots, n, \quad (7)$$

where $\mathbf{x}_{a,p}$, $\mathbf{x}_{t,p}$, and $\mathbf{x}_{r,p}$ are the a priori, true, and retrieved NH_3 vertical mole fraction profiles, respectively; TC_a and TC_r are the a priori and retrieved NH_3 column, respectively, in units of molecules cm^{-2}; $\mathbf{PC}_a$ and $\mathbf{PC}_t$ are the a priori and true partial column vertical profiles of NH_3, respectively, in a unit of molecules cm^{-2}; **CAVK** is the column averaging kernel in units of (molecules cm^{-2}) (molecules $cm^{-2})^{-1}$; $\mathbf{PC}_{air}$ is the partical column vertical profile of the dry air.

Figures 4b and 4c show a typical averaging kernel (**AVK**) of HIRAS retrieved NH_3 over land and ocean. Due

to the weak absorption lines and low concentrations of NH_3, the retrieved HIRAS NH_3 column is mainly sensitive to the mid-troposphere (2–8 km), which is similar to GOSAT and TES satellite retrievals (Clarisse et al., 2010; Someya et al., 2020). The NH_3 mole fraction is high in the boundary layer (0–2 km), but it also shows relatively high values in the mid-troposphere (2–6 km; Fig. 4a), especially over land. Consequently, such an **AVK** still allows us to derive NH_3 column information. Note that the **AVK** value varies strongly with surface type and atmospheric conditions. For instance, the NH_3 signals captured by HIRAS over the ocean are very weak leading to a degree of freedom (DOFs) close to 0, and the DOFs can be up to 0.9 over several polluted land areas.

3. Results

3.1. *NH_3 global map*

As an example, Fig. 5 shows the NH_3 global maps observed by the HIRAS satellite during daytime and nighttime on 30 January 2020. Note that we filter out the retrieved NH_3 columns with a DOF < 0.2, root mean square error of the fitting residual (RMSE) > 0.55%, and an NH_3 column < 0. More valid NH_3 column data are available over land than over the ocean. Moreover, the uncertainty of the NH_3 retrievals is relatively large during the nighttime as compared to the daytime, because the NH_3 retrieval quality depends on the thermal contrast between the surface and the lowest atmospheric layer; therefore, it is more challenging to capture the NH_3 signal near the surface when the thermal contrast is small during nighttime (Clarisse et al., 2010).

The HIRAS measurements show several NH_3 hotspots around the world, e.g., India, West Africa, and East China. These hotspots observed in the HIRAS data are generally consistent with the CAMS model simulations (Fig. 3) since there are large NH_3 emissions in these regions (Stein et al., 2014). Compared to the CAMS model monthly means between 2015 and 2020, the HIRAS retrieved NH_3 columns during the daytime on 30 January 2020 are larger than the model simulations in middle Africa and lower than the model simulations in East China.

3.2. *Comparison with IASI measurements*

To assess the uncertainty of the HIRAS NH_3 retrievals, we compare HIRAS with IASI/Metop-B NH_3 measurements. The IASI measurements have been validated with nine ground-based FTIR sites around the world, and the relative means and stds of the differences (IASI – FTIR) are –32.4% ±56.3% (Dammers et al., 2016). Figures 6 and 7 show the global monthly NH_3 columns during daytime observed by HIRAS and IASI satellites in January and July 2020, respectively. The HIRAS and IASI data pairs are selected based on their co-located gridded monthly values. Although HIRAS provides lower data density than IASI, especially over the ocean and in the high-latitude regions, the two satellites see a similar global map of NH_3 columns. High NH_3 columns are observed in regions with high human activities or strong biomass burnings, which agrees well with bottom-up emission inventories (Crippa et al., 2020).

Six regions (North America, Europe, East China, South America, Africa, and India) are selected to investigate the correlations and relative differences between HIRAS and IASI NH_3 monthly mean columns (Table 2). Positive correlations between both satellite data sets are identified in all these regions, with the Pearson correlation coefficient (R) ranging

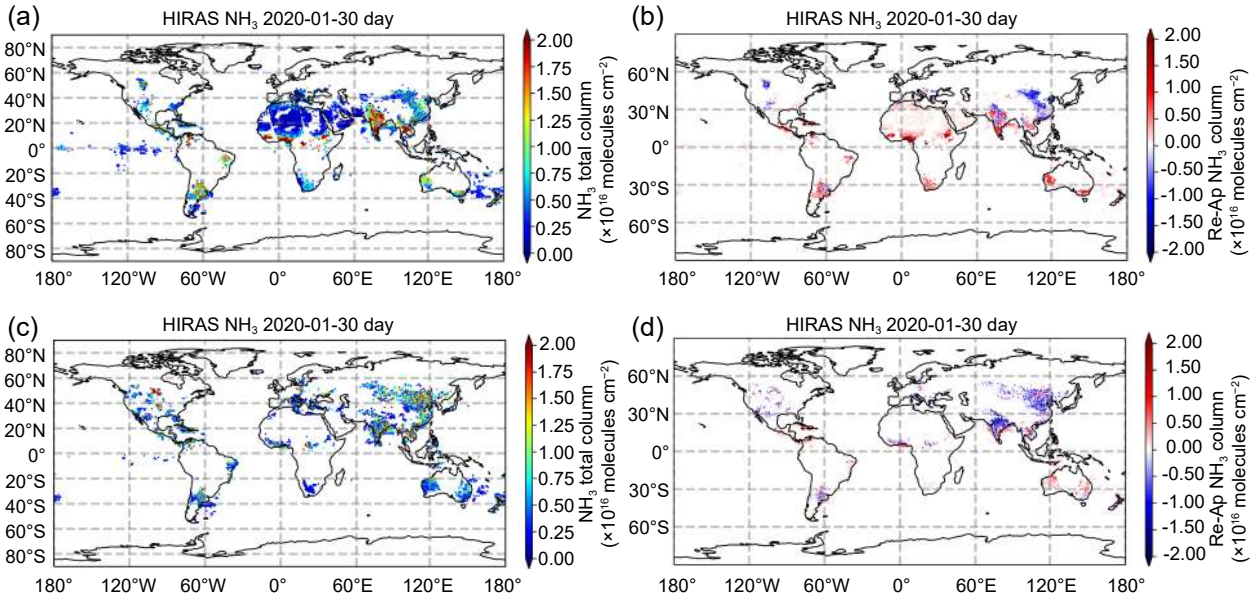

Fig. 5. The retrieved NH_3 columns on 30 January 2020 from the HIRAS observations under clear-sky conditions during daytime (a) and nighttime (c), together with the differences between the retrieved columns and a priori columns (re-ap) during daytime (b) and nighttime (d), respectively.

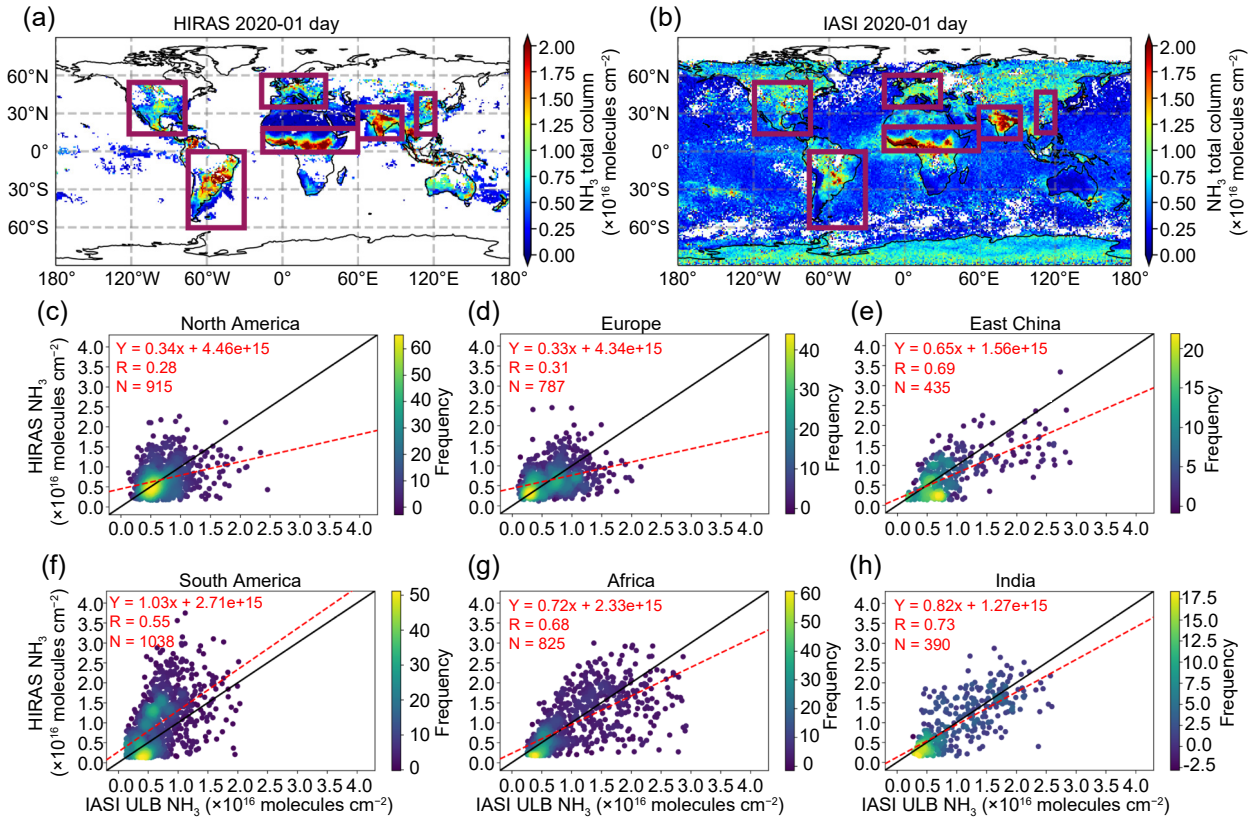

Fig. 6. The NH_3 column monthly means in January 2020 observed by (a) HIRAS/FY3D and (b) IASI/MetopB re-gridded onto 1° × 1° (latitude × longitude). The scatter plots between HIRAS and IASI NH_3 columns in (c) North America, (d) Europe, (e) East China, (f) South America, (g) Africa, and (h) India. In each scatter plot, the dots are colored according to the data density. The red dashed line is the linear regression. The solid black line is the one-to-one line. *R* is the Pearson correlation coefficient and *N* is the number of the data points.

from 0.28 to 0.73 in January, and from 0.31 to 0.58 in July. The *R* values are relatively lower in July as compared to those in January, especially in East China, Africa, and India, because the HIRAS has significantly fewer clean-sky pixels in these regions after the cloud filtering. Table 2 shows the means and standard deviations (stds) of the differences between HIRAS and IASI NH_3 columns. In January, the mean relative differences (HIRAS-IASI) are within 5.5% in North America, Europe, Africa, and India, –17.2% in East China, and 35.6% in South America. The stds of their relative differences are between 46.6% and 82.4%. In July, the mean relative differences (HIRAS – IASI) are within 12% in Europe, East China, Africa, India, and 42.5% in South America. The stds of their relative differences are between 51.8% and 82.3%. These values are comparable to the means and stds of the differences between IASI and ground-based FTIR measurements.

4. Discussion

Currently, the HIRAS satellite after quality filtering provides a smaller data density than the IASI, and the HIRAS NH_3 measurements are mainly over land and in mid- and low-latitude regions. Figure 8 shows all the convergent retrievals derived from the HIRAS spectra in January 2020 before applying the RMSE and DOF filtering. We found a strong latitudinal dependence in terms of the RMSE, with relatively low values in low-latitude regions and high values in high-latitude regions. Figure 9 illustrates the relationship between the RMSE and DOF of HIRAS NH_3 retrievals in January 2020 and latitude. Similar to Fig. 8, we find that the RMSE is pretty large and the DOF is generally less than 0.05 in the high-latitude regions. The SNR of HIRAS spectra is low in high-latitude regions, which is probably caused by low surface temperatures and significant snow coverage. With our quality filtering criteria, the HIRAS NH_3 retrievals in the high-latitude regions are mainly filtered out. In Fig. 8b, several areas in the tropics and near the Inter-tropical Convergence Zone (ITCZ; Waliser and Gautier, 1993) still have a relatively high RMSE which indicates remaining cloud effects. Therefore, an improved cloud screening method is needed in the future to better select clear-sky HIRAS measurements. For example, we could apply the nitrous oxide (N_2O) infrared absorption lines to retrieve cloud parameters and to do a cloud mask (Siddans et al., 2017), or design a new cloud detection algorithm based on a neural network (Whitburn et al., 2022). Apart from the ITCZ regions, there is no obvious RMSE difference

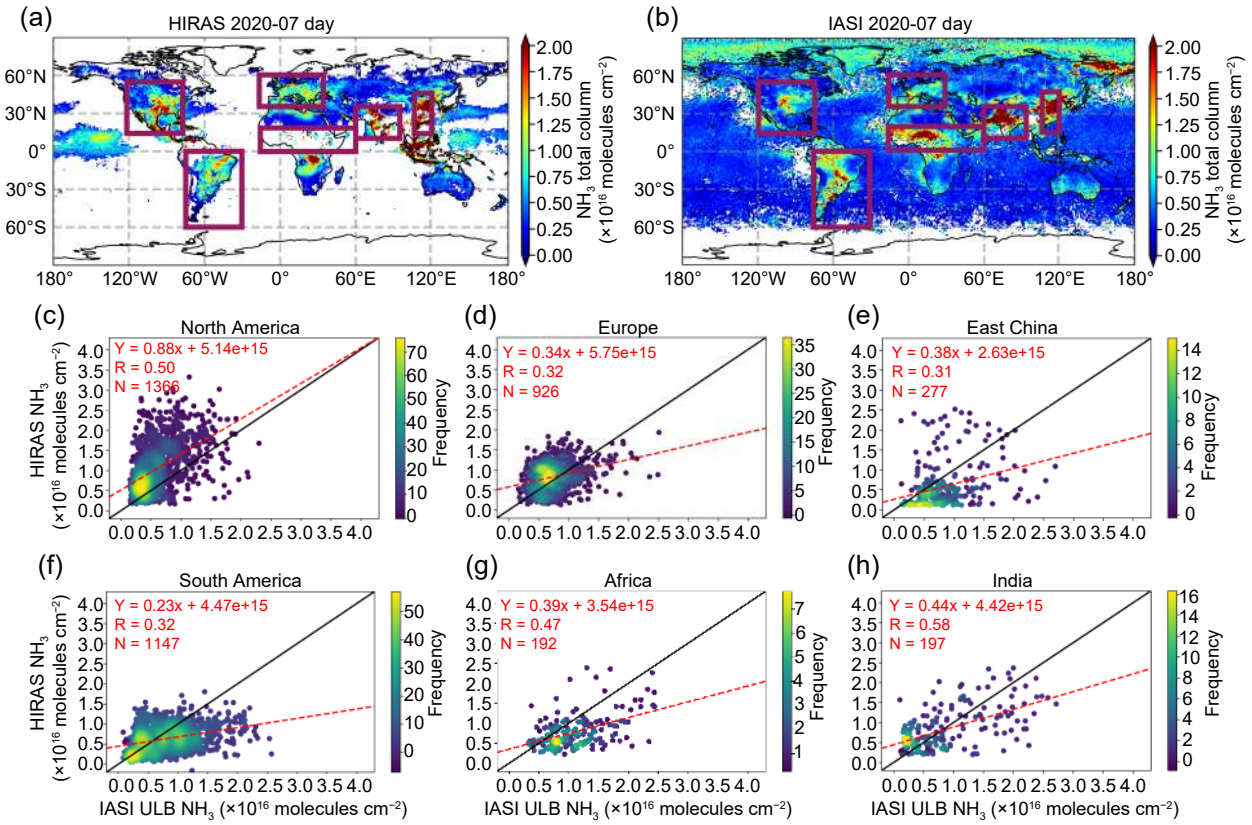

Fig. 7. Same as Fig. 6, but for July 2020.

Table 2. The relative mean and std of the difference between HIRAS and IASI measurements [(HIRAS−IASI)/IASI × 100%] over six regions with high NH_3 columns in January and July 2020, together with their Pearson correlation coefficients (R), p-values, and mean DOFs.

		Region (latitude/longitude)					
		North America [15°N, 55°N]/ [120°W, 80°W]	Europe [30°N, 60°N]/ [20°W, 30°E]	East China [15°N, 45°N]/ [100°E, 120°E]	South America [60°S, 0°]/ [80°W, 30°W]	Africa [0°, 18°N]/ [20°W, 60°E]	India [10°N, 35°N]/ [60°E, 90°E]
Jan-2020	Mean (%)	–2.0	–3.1	–17.2	35.6	–5.5	–5.2
	Std (%)	52.9	65.1	65.1	82.4	51.7	46.6
	R	0.28	0.31	0.69	0.55	0.68	0.73
	P-value	<0.001	<0.001	<0.001	<0.001	<0.001	<0.001
	DOF	0.47	0.48	0.61	0.53	0.49	0.57
Jul-2020	Mean (%)	42.5	11.4	–3.0	–9.9	–11.0	–3.6
	Std (%)	78.7	53.4	82.3	71.5	51.8	60.8
	R	0.50	0.32	0.31	0.32	0.47	0.58
	P-value	<0.001	<0.001	<0.001	<0.001	<0.001	<0.001
	DOF	0.57	0.66	0.44	0.45	0.42	0.54

between land and ocean retrievals in tropical areas. However, we find that the DOF over the ocean is quite low even with a low RMSE. The reason is that the NH_3 concentration over the ocean is so low that the NH_3 signal is too weak to be captured from the HIRAS observed spectra. Regarding the HIRAS measurements in the high-latitude regions, the RMSE is generally larger than 0.5%, leading to a low DOF as well. Overall, for all the retrievals with a low DOF due to a bad fitting or a low NH_3 column, the retrieved NH_3 columns are pretty close to their a priori values as the retrieval is dominated by the a priori information (Rodgers, 2000).

To better understand why there are almost no HIRAS NH_3 retrievals left over the ocean after quality filtering, we have applied our retrieval algorithm developed for HIRAS (section 2) to IASI L1C data. Figure 10 shows typical spectra over the ocean derived from two adjacent HIRAS and IASI observations on 30 January 2020, respectively. Note that the

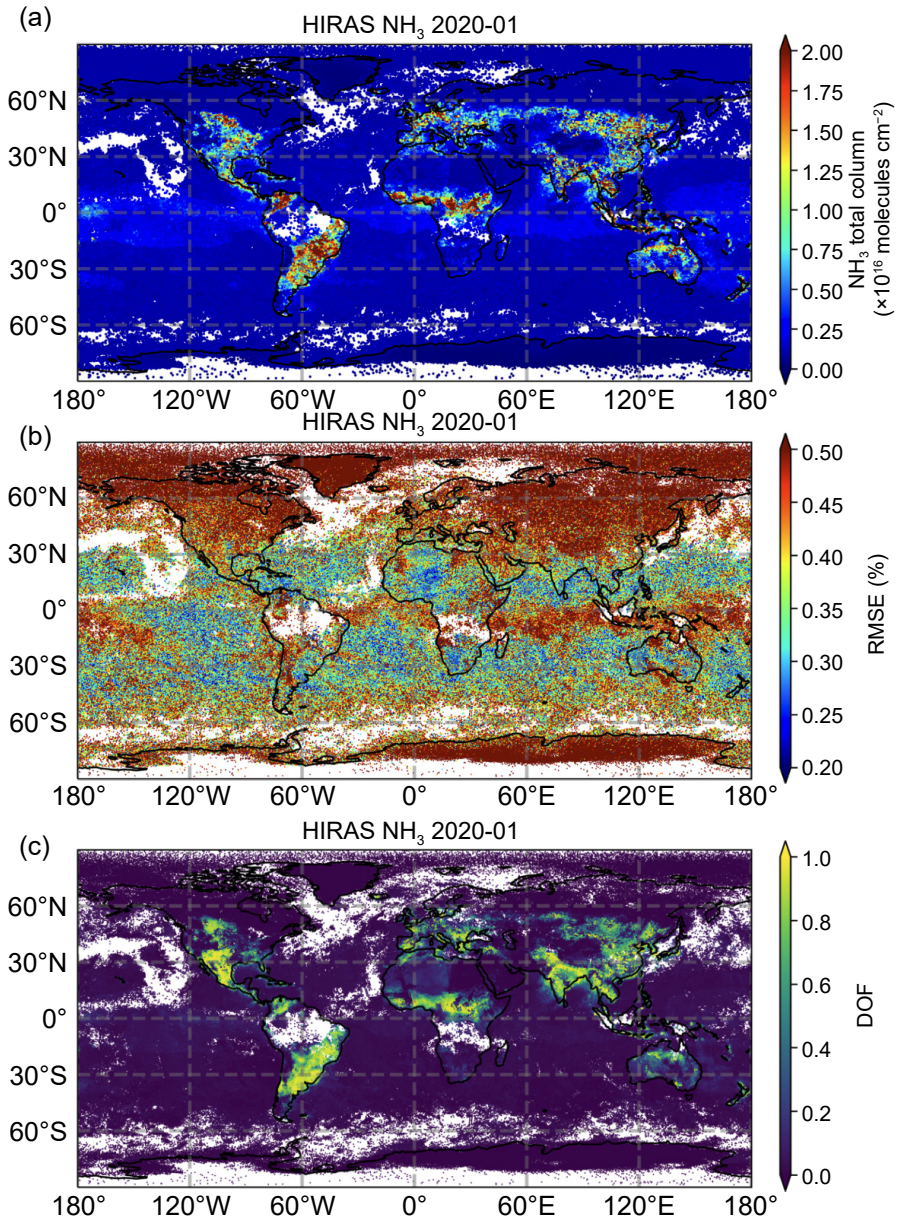

Fig. 8. (a) The NH_3 columns, (b), the RMSE, and (c) the DOF for all convergent retrievals derived from the HIRAS spectra in January 2020.

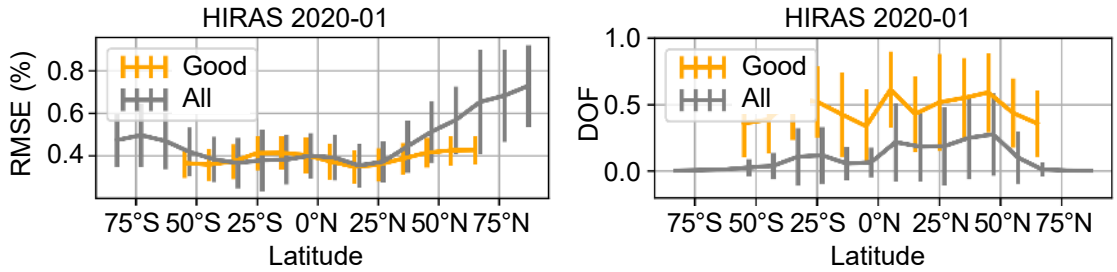

Fig. 9. The RMSE (left) and DOF (right) as a function of the latitude bin (every 10 degrees) as derived from all the HIRAS NH_3 retrievals (grey) and the retrievals after quality filtering (orange) in January 2020. The error bar is the standard deviation.

same a priori profiles coming from the CAMS model are used for the HIRAS and IASI NH_3 retrievals. Both retrievals are convergent. However, the DOF of the retrieved NH_3 column from the HIRAS spectrum is very

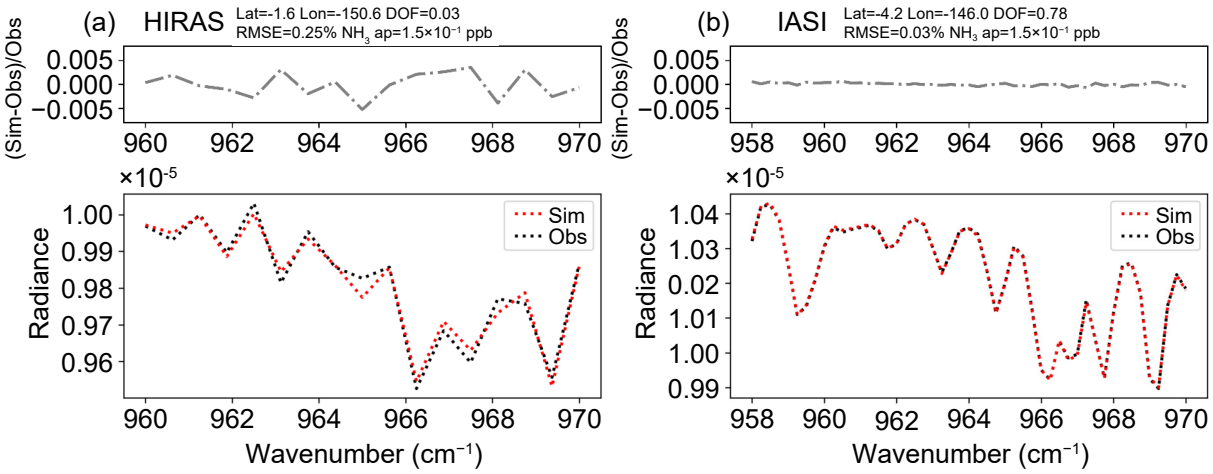

Fig. 10. Typical NH_3 retrievals over the ocean using the (a) HIRAS observed spectrum and (b) the IASI observed spectrum. Note that the a priori NH3 in the title denotes the NH_3 mole fraction near the surface.

low (DOF = 0.03) causing the retrieved NH_3 column to be almost the same as the a priori column. The RMSE of the IASI residual is 0.03%, which is about eight times better than that of the HIRAS retrieval (0.25%). Thanks to the high SNR, we can successfully retrieve the NH_3 column (DOF = 0.78) from the IASI spectrum. This experiment demonstrates that the SNR of the HIRAS spectrum is currently too weak to derive the NH_3 column above regions with a low NH_3 column, such as the ocean.

5. Conclusions

In this study, a retrieval (algorithm and strategy) based on the optimal estimation method is established to derive the NH_3 column from the LWIR nadir radiance spectra measured by HIRAS onboard the FY-3D satellite. We use the ASIMUT atmospheric radiative transfer model as the forward model to simulate the thermal radiation emitted from the surface and the atmosphere. The CAMS model is applied to create the a priori information of NH_3. The retrieval window of 960–970 cm^{-1} is carefully selected to perform NH_3 column retrievals from the HIRAS spectra.

The first global map of atmospheric NH_3 columns observed by the HIRAS/FY-3D satellite shows several NH_3 hotspots around the world, for example, India, West Africa, and East China, where there are large NH_3 emissions (Stein et al., 2014). The HIRAS NH_3 columns are also compared to IASI observations. Both satellites observe similar NH_3 column spatial distributions. In January 2020, the mean relative differences are within 5.5% in North America, Europe, Africa, and India, –17.2% in East China, and 35.6% in South America. The stds of their relative differences are between 46.6% and 82.4%. In July 2020, the mean relative differences are within 12% in Europe, East China, Africa, India, and 42.5% in South America. The stds of their relative differences are between 51.8% and 82.3%. These values are comparable to the differences between IASI data and collocated reference ground-based FTIR data.

Finally, the remaining issues in the HIRAS NH_3 retrievals are discussed:

1) the SNR of the HIRAS spectrum in the high-latitude regions is too weak to perform NH_3 retrieval;

2) an improved cloud screening method is needed to better select clear-sky HIRAS pixels, especially near the ITCZ;

3) the SNR of the HIRAS spectrum is currently too low to derive reliable NH_3 columns for regions with a very low NH_3 column, even in low-latitude areas such as the tropical oceans.

Acknowledgements. The authors would like to thank Ann Carine VANDAELE (BIRA-IASB) for supporting the ASIMUT model. This study is supported by the FengYun Application Pioneering Project (FY-APP-2022.0502) and the National Natural Science Foundation of China (Grant No. 42205140).

Data availability. The HIRAS Level 1 data is publicly available via https://www.nsmc.org.cn/. The CAMS NH_3 model is publicly available via https://ads.atmosphere.copernicus.eu/cdsapp#!/dataset/cams-global-reanalysis-eac4?tab=overview. The IASI NH_3 data are publicly available at https://iasi.aeris-data.fr/. The IASI L1C data are provided by the EUMETSAT https://navigator.eumetsat.int/. The HIRAS NH_3 retrievals are available upon request to the authors.

REFERENCES

NOAA., 1976: *U.S. Standard Atmosphere, 1976*. United States Committee on Extension to the Standard Atmosphere, 227 pp.

Bao, Z. E., and Coauthors, 2021: Effects of NH_3 on secondary aerosol formation from toluene/NOx photo-oxidation in different O_3 formation regimes. *Atmos. Environ.*, **261**, 118603, https://doi.org/10.1016/j.atmosenv.2021.118603.

Behera, S. N., M. Sharma, V. P. Aneja, and R. Balasubramanian, 2013: Ammonia in the atmosphere: A review on emission sources, atmospheric chemistry and deposition on terrestrial bodies. *Environmental Science and Pollution Research*, **20**, 8092–8131, https://doi.org/10.1007/s11356-013-2051-9.

Bouwman, A. F., D. S. Lee, W. A. H. Asman, F. J. Dentener, K. W. Van Der Hoek, and J. G. J. Olivier, 1997: A global high-resolution emission inventory for ammonia. *Global Biogeochemical Cycles*, **11**, 561–587, https://doi.org/10.1029/97GB02266.

Clarisse, L., C. Clerbaux, F. Dentener, D. Hurtmans, and P.-F. Coheur, 2009: Global ammonia distribution derived from infrared satellite observations. *Nature Geoscience*, **2**, 479–483, https://doi.org/10.1038/ngeo551.

Clarisse, L., and Coauthors, 2010: Satellite monitoring of ammonia: A case study of the San Joaquin Valley. *J. Geophys. Res. Atmos.*, **115**, D13302, https://doi.org/10.1029/2009JD013291.

Crippa, M., and Coauthors, 2020: High resolution temporal profiles in the emissions database for global atmospheric research. *Scientific Data*, **7**, 121, https://doi.org/10.1038/s41597-020-0462-2.

Dammers, E., and Coauthors, 2016: An evaluation of IASI-NH_3 with ground-based Fourier transform infrared spectroscopy measurements. *Atmospheric Chemistry and Physics*, **16**, 10 351–10 368, https://doi.org/10.5194/acp-16-10351-2016.

Dammers, E., and Coauthors, 2017: Validation of the CrIS fast physical NH_3 retrieval with ground-based FTIR. *Atmospheric Measurement Techniques*, **10**, 2645–2667, https://doi.org/10.5194/amt-10-2645-2017.

De Wachter, E., N. Kumps, A. C. Vandaele, B. Langerock, and M. De Mazière, 2017: Retrieval and validation of MetOp/IASI methane. *Atmospheric Measurement Techniques*, **10**, 4623–4638, https://doi.org/10.5194/amt-10-4623-2017.

Gordon, I. E., and Coauthors, 2022: The HITRAN2020 molecular spectroscopic database. *Journal of Quantitative Spectroscopy and Radiative Transfer*, **277**, 107949, https://doi.org/10.1016/j.jqsrt.2021.107949.

Guo, Y. X., and Coauthors, 2020: Air quality, nitrogen use efficiency and food security in China are improved by cost-effective agricultural nitrogen management. *Nature Food*, **1**, 648–658, https://doi.org/10.1038/s43016-020-00162-z.

Hao, L. Q., E. Kari, A. Leskinen, D. R. Worsnop, and A. Virtanen, 2020: Direct contribution of ammonia to α-pinene secondary organic aerosol formation. *Atmospheric Chemistry and Physics*, **20**, 14 393–14 405, https://doi.org/10.5194/acp-20-14393-2020.

Hersbach, H., and Coauthors, 2020: The ERA5 global reanalysis. *Quart. J. Roy. Meteor. Soc.*, **146**, 1999–2049, https://doi.org/10.1002/qj.3803.

Hilton, F., and Coauthors, 2012: Hyperspectral earth observation from IASI: Five years of accomplishments. *Bull. Amer. Meteor. Soc.*, **93**, 347–370, https://doi.org/10.1175/BAMS-D-11-00027.1.

Inness, A., and Coauthors, 2019: The CAMS reanalysis of atmospheric composition. *Atmospheric Chemistry and Physics*, **19**, 3515–3556, https://doi.org/10.5194/acp-19-3515-2019.

Kaiser, J. W., and Coauthors, 2012: Biomass burning emissions estimated with a global fire assimilation system based on observed fire radiative power. *Biogeosciences*, **9**, 527–554, https://doi.org/10.5194/bg-9-527-2012.

Li, S. Q., H. Hu, C. G. G. Fang, S. C. Wang, S. P. Xun, B. F. He, W. Y. Wu, and Y. F. Huo, 2022: Hyperspectral infrared atmospheric sounder (HIRAS) atmospheric sounding system. *Remote Sensing*, **14**, 3882, https://doi.org/10.3390/rs14163882.

Luo, Z. Q., Y. Z. Zhang, W. Chen, M. Van Damme, P.-F. Coheur, and L. Clarisse, 2022: Estimating global ammonia (NH_3) emissions based on IASI observations from 2008 to 2018. *Atmospheric Chemistry and Physics*, **22**, 10 375–10 388, https://doi.org/10.5194/acp-22-10375-2022.

Mahowald, N. M., R. Scanza, J. Brahney, C. L. Goodale, P. G. Hess, J. K. Moore, and J. Neff, 2017: Aerosol deposition impacts on land and ocean carbon cycles. *Current Climate Change Reports*, **3**, 16–31, https://doi.org/10.1007/s40641-017-0056-z.

Mishchenko, M. I., and L. D. Travis, 1998: Capabilities and limitations of a current FORTRAN implementation of the *T*-matrix method for randomly oriented, rotationally symmetric scatterers. *Journal of Quantitative Spectroscopy and Radiative Transfer*, **60**, 309–324, https://doi.org/10.1016/S0022-4073(98)00008-9.

Na, K., C. Song, C. Switzer, and D. R. Cocker, 2007: Effect of ammonia on secondary organic aerosol formation from α-pinene ozonolysis in dry and humid conditions. *Environ. Sci. Technol.*, **41**, 6096–6102, https://doi.org/10.1021/es061956y.

Qi, C. L., and Coauthors, 2020: High spectral infrared atmospheric sounder (HIRAS): System overview and on-orbit performance assessment. *IEEE Trans. Geosci. Remote Sens.*, **58**, 4335–4352, https://doi.org/10.1109/TGRS.2019.2963085.

Rodgers, C. D., 2000: *Inverse Methods for Atmospheric Sounding: Theory and Practice*. World Scientific, 256 pp. https://doi.org/10.1142/3171.

Shephard, M. W., and K. E. Cady-Pereira, 2015: Cross-track infrared sounder (CrIS) satellite observations of tropospheric ammonia. *Atmospheric Measurement Techniques*, **8**, 1323–1336, https://doi.org/10.5194/amt-8-1323-2015.

Siddans, R., D. Knappett, B. Kerridge, A. Waterfall, J. Hurley, B. Latter, H. Boesch, and R. Parker, 2017: Global height-resolved methane retrievals from the infrared atmospheric sounding interferometer (IASI) on MetOp. *Atmospheric Measurement Techniques*, **10**, 4135–4164, https://doi.org/10.5194/amt-10-4135-2017.

Sindelarova, K., and Coauthors, 2014: Global data set of biogenic VOC emissions calculated by the MEGAN model over the last 30 years. *Atmospheric Chemistry and Physics*, **14**, 9317–9341, https://doi.org/10.5194/acp-14-9317-2014.

Someya, Y., R. Imasu, K. Shiomi, and N. Saitoh, 2020: Atmospheric ammonia retrieval from the TANSO-FTS/GOSAT thermal infrared sounder. *Atmospheric Measurement Techniques*, **13**, 309–321, https://doi.org/10.5194/amt-13-309-2020.

Spurr, R., 2008: LIDORT and VLIDORT: Linearized pseudo-spherical scalar and vector discrete ordinate radiative transfer models for use in remote sensing retrieval problems. *Light Scattering Reviews 3: Light Scattering and Reflection*, A. A. Kokhanovsky, Ed., Springer, 229–275. https://doi.org/10.1007/978-3-540-48546-9_7.

Stein, O., M. G. Schultz, I. Bouarar, H. Clark, V. Huijnen, A. Gaudel, M. George, and C. Clerbaux, 2014: On the wintertime low bias of Northern Hemisphere carbon monoxide found in global model simulations. *Atmospheric Chemistry and Physics*, **14**, 9295–9316, https://doi.org/10.5194/acp-14-9295-2014.

Twigg, M. M., and Coauthors, 2022: Intercomparison of in situ measurements of ambient NH_3: Instrument performance and application under field conditions. *Atmospheric Measurement Techniques*, **15**, 6755–6787, https://doi.org/10.5194/amt-15-

6755-2022.

Van Damme, M., J. W. Erisman, L. Clarisse, E. Dammers, S. Whitburn, C. Clerbaux, A. J. Dolman, and P.-F. Coheur, 2015: Worldwide spatiotemporal atmospheric ammonia (NH_3) columns variability revealed by satellite. *Geophys. Res. Lett.*, **42**, 8660–8668, https://doi.org/10.1002/2015GL065496.

Van Damme, M., L. Clarisse, S. Whitburn, J. Hadji-Lazaro, D. Hurtmans, C. Clerbaux, and P.-F. Coheur, 2018: Industrial and agricultural ammonia point sources exposed. *Nature*, **564**, 99–103, https://doi.org/10.1038/s41586-018-0747-1.

Vandaele, A. C., M. Kruglanski, and M. De Mazière, 2006: Modeling and retrieval of atmospheric spectra using ASIMUT. *Proc. of the First "Atmospheric Science Conference"*, Vol. ESA SP-628, July 2006, Frascati, Italy.

Vandenbussche, S., S. Kochenova, A. C. Vandaele, N. Kumps, and M. De Mazière, 2013: Retrieval of desert dust aerosol vertical profiles from IASI measurements in the TIR atmospheric window. *Atmospheric Measurement Techniques*, **6**, 2577–2591, https://doi.org/10.5194/amt-6-2577-2013.

Waliser, D. E., and C. Gautier, 1993: A satellite-derived climatology of the ITCZ. *J. Climate*, **6**, 2162–2174, https://doi.org/10.1175/1520-0442(1993)006<2162:ASDCOT>2.0.CO;2.

Wang, R., and Coauthors, 2021: Monthly patterns of ammonia over the contiguous United States at 2 - km resolution. *Geophys. Res. Lett.*, **48**, e2020GL090579, https://doi.org/10.1029/2020GL090579.

Whitburn, S., L. Clarisse, M. Crapeau, T. August, T. Hultberg, P. F. Coheur, and C. Clerbaux, 2022: A CO_2-independent cloud mask from Infrared atmospheric sounding interferometer (IASI) radiances for climate applications. *Atmospheric Measurement Techniques*, **15**, 6653–6668, https://doi.org/10.5194/amt-15-6653-2022.

Wu, C. Q., and Coauthors, 2020: FY-3D HIRAS radiometric calibration and accuracy assessment. *IEEE Trans. Geosci. Remote Sens.*, **58**, 3965–3976, https://doi.org/10.1109/TGRS.2019.2959830.

Xian, D., P. Zhang, L. Gao, R. J. Sun, H. Z. Zhang, and X. Jia, 2021: Fengyun meteorological satellite products for earth system science applications. *Adv. Atmos. Sci.*, **38**, 1267–1284, https://doi.org/10.1007/s00376-021-0425-3.

Xu, L., and J. E. Penner, 2012: Global simulations of nitrate and ammonium aerosols and their radiative effects. *Atmospheric Chemistry and Physics*, **12**, 9479–9504, https://doi.org/10.5194/acp-12-9479-2012.

Yang, Z. D., and Coauthors, 2019: Capability of *Fengyun-3D* satellite in earth system observation. *J. Meteor. Res.*, **33**, 1113–1130, https://doi.org/10.1007/s13351-019-9063-4.

Zhang, C. M., M. J. Gu, Y. Hu, P. Y. Huang, T. H. Yang, S. Huang, C. L. Yang, and C. Y. Shao, 2021: A study on the retrieval of temperature and humidity profiles based on FY-3D/HIRAS infrared hyperspectral data. *Remote Sensing*, **13**, 2157, https://doi.org/10.3390/rs13112157.

Zhou, D. K., A. M. Larar, X. Liu, W. L. Smith, L. L. Strow, P. Yang, P. Schlüssel, and X. Calbet, 2011: Global land surface emissivity retrieved from satellite ultraspectral IR measurements. *IEEE Trans. Geosci. Remote Sens.*, **49**, 1277–1290, https://doi.org/10.1109/TGRS.2010.2051036.

Zhu, L. Y., D. K. Henze, J. O. Bash, K. E. Cady-Pereira, M. W. Shephard, M. Luo, and S. L. Capps, 2015: Sources and impacts of atmospheric NH_3: Current understanding and frontiers for modeling, measurements, and remote sensing in North America. *Current Pollution Reports*, **1**, 95–116, https://doi.org/10.1007/s40726-015-0010-4.